Electronic Research Archive

ERA, 34(5): 3289–3314.
DOI: 10.3934/era.2026148
Received: 09 February 2026
Revised: 19 March 2026
Accepted: 02 April 2026
Published: 15 April 2026

https://www.aimspress.com/journal/ERA

Research article

Filtering regulation of synchronization and energy balance in functional memristor networks

Jingjing Yang, Suyuan Huang, Yuan Chai*, Shunmin Yao and Rui Zhu

School of Mathematics and Physics, Shanghai University of Electric Power, Shanghai 201306, China

* **Correspondence:** Email: chaiyuan@shiep.edu.cn.

Abstract: The frequency-selective response of the nervous system bears a strong resemblance to filtering mechanisms. However, how concurrent cross-modal filtering influences neuronal synchronization remains unclear. This study constructed a coupled photosensitive-auditory neuron model incorporating flux-controlled memristors. Through inductive coil connections, we investigated its synchronous dynamics under frequency-swept signal excitation. The key innovation lies in simultaneously applying swept chirp excitation to both light and sound inputs, achieving biophysically plausible bandpass filtering based on the intrinsic frequency tuning of sensory pathways, while employing an adaptive coupling strategy based on Hamiltonian energy differences. Results demonstrate that bimodal filtering significantly enhances frequency-dependent synchronization. When the sweeping signal traverses the dual passbands, the system exhibits robust synchronization characterized by phase locking and energy minimization, significantly outperforming unfiltered or unimodal conditions. This study reveals cross-modal collaborative filtering as a fundamental mechanism for neural synchronization, providing a computational framework for multisensory integration. It offers significant implications for developing novel neural prostheses synchronized by photoacoustic cues.

Keywords: FitzHugh-Nagumo model; photosensitive neurons; auditory neurons; memristor; wave filtering

1. Introduction

The modeling of neuronal electrical activity originated from the Hodgkin-Huxley (HH) model [1–3]. Although complex, this model has been employed in network-level studies, and its complexity has subsequently driven the development of more simplified models. Subsequently developed spiking models, including the resistor-capacitor (RC) circuit and other models, provide simplified frameworks for simulating neuronal firing patterns [4–6]. The FitzHugh-Nagumo (FHN) model, derived from the HH model during 1961–1963, maintains fundamental action potential characteristics while significantly reducing computational complexity. Its equivalent circuit comprises external voltage/current sources, linear resistors, nonlinear resistors, capacitors, and inductors [7,8]. Incorporating specialized components like phototransistors, piezoelectric ceramics, or thermistors into the basic FHN circuit enables targeted simulation of functionally specific neurons, including photosensitive [9–11], auditory [12], and thermal neurons [13].

The FHN model incorporating phototube elements simulates photosensitive neurons' light-dependent firing activity, serving as fundamental units for optoelectronic signal conversion and transmission [14,15]. With piezoelectric ceramic components, the model implements auditory neurons that transduce sound signals via piezoelectric effects for mechano-electrical energy conversion [16]. Thermal perception in FHN-based neurons utilizes thermistors to detect ambient temperature variations and convert them into electrical signals [17–19]. Since biological neural systems inherently process multisensory information, investigating coupled dynamics between photosensitive, auditory, and thermal neuronal models becomes crucial for replicating multimodal processing capabilities [20–22].

Therefore, the first part of this work studies the simulation of neuronal firing behavior in the FHN model, focusing on the case where coupling is carried out between different functional neurons by connecting two different FHN neuronal circuits and adding the effect of noise to examine the firing and synchronization of functional neurons. As a special electronic component characterized by biomimetic properties, nonvolatility, low power consumption, and programmability, the memristor is analogous to the synapses of biological neurons, as it is able to simulate the connection and information transfer between neurons. In recent years, many studies have focused on connecting the memristors with neuronal circuits [23–25], which can effectively simulate behaviors including spike burst behavior, chaotic spike behavior, and discharge pattern transitions. Alternatively, memristive resistors were introduced into coupled channels between functional neurons [26,27] to effectively generate rich dynamic behaviors and higher firing frequencies, and to show the effectiveness of memristive resistors as electrically coupled synapses. However, most of these studies have primarily focused on the rich firing dynamics induced by external stimulation, with few investigating the direct interaction between stimuli and neurons via the series connection of memristors as nonlinear resistors within functional neuronal circuits.

The second part of the work in this paper is to connect a magnetic flux memristor as a nonlinear element in series to the voltage source branch of a photosensitive neuron so that the effect of membrane potential-induced electromagnetic fields on the coupling of functional neurons can be examined. In addition, phototubes and piezoelectric ceramics enable frequency-selective filtering of external signals through configurable filtering criteria, generating continuous electrical stimulation in neural circuits. This allows controlled modulation of photocurrents and piezoelectric currents based on predefined frequency parameters. Recent neuronal modeling studies have implemented such filtering techniques, including preprocessing external inputs to individual neurons [28] and employing signals of specific

frequency bands as external stimuli in nonlinear coupling investigations [29].

Moreover, at the single-neuron level, studies have demonstrated that neurons inherently possess frequency-selective filtering properties, with their optimal responsiveness depending on the matching between stimulus frequency and intrinsic frequency [30]. At the sensory information processing level, membrane filtering has been shown to be a key mechanism for encoding complex signals such as amplitude-modulated (AM) sounds [31]. However, these studies have focused on single-modality or single-neuron systems. How concurrent filtering across sensory modalities collaboratively regulates the synchronous dynamics of function-specific neurons remains a key question yet to be thoroughly explored. Specifically, a crucial step in elucidating the neural mechanisms of multisensory integration is to understand how the synchronous behavior of a coupled photosensitive-auditory neuron system responds to variations in filtering parameters. This is investigated under the condition where each neuron receives an external linear frequency-swept (chirp) signal that has been preprocessed by frequency-selective filtering.

Therefore, the third part of this study aims to investigate the regulatory mechanism of cross-modal filtering on the synchronized dynamics of heterogeneous neuronal coupling. Using photosensitive neurons and auditory neurons as models, we systematically analyze how filtering parameters (such as passband frequency) and coupling parameters synergistically influence the process of synchronization (e.g., synchronization time and phase relationships), thereby revealing the cellular basis of multisensory integration. The main innovations of this work are as follows:

1) A coupled photosensitive-auditory neuron model incorporating flux-controlled memristors is introduced, providing a dynamically tunable computational platform for simulating biologically realistic cross-modal interactions;

2) A dual-mode concurrent filtering strategy based on swept-frequency signals is proposed, revealing the pivotal role of frequency-selective filtering in inducing robust synchronization;

3) This study elucidates the regulatory mechanisms of key parameters in the synchronization process, providing a theoretical basis for parameter optimization in frequency-dependent neural modulation techniques.

The structure of this paper is as follows. Section 2 first constructs and analyzes the dynamic characteristics of basic photosensitive neurons, auditory neurons, and novel flux memristive photosensitive neurons. Based on this, the optimized flux photosensitive neurons are dynamically coupled with auditory neurons to investigate the impact of electromagnetic interactions on system dynamics. Section 3 focuses on the cross-modal filtering synchronization mechanism under swept-frequency signals: Part 1 reveals the advantages of dual-mode filtering in inducing fast and robust synchronization through systematic comparisons of different filtering modes; and Part 2 quantitatively analyzes the influence patterns of key parameters on synchronization dynamics under optimal filtering conditions. Finally, conclusions are summarized.

2. Model and scheme

This paper is based on the FHN neuron model, which combines capacitance, inductance, linear resistance, and nonlinear resistance to form equivalent neural circuits that can reproduce the energy properties of biological neurons.

2.1. Modeling of isolated photosensitive neurons

The phototube in the photosensitive neuron model can capture electromagnetic waves in a specific frequency band, and when irradiated by high-frequency external irradiation that exceeds a threshold value determined by the cathode material, the phototube will enable photoelectric conversion; the functional neural circuit coupled by the phototube is shown in Figure 1(a).

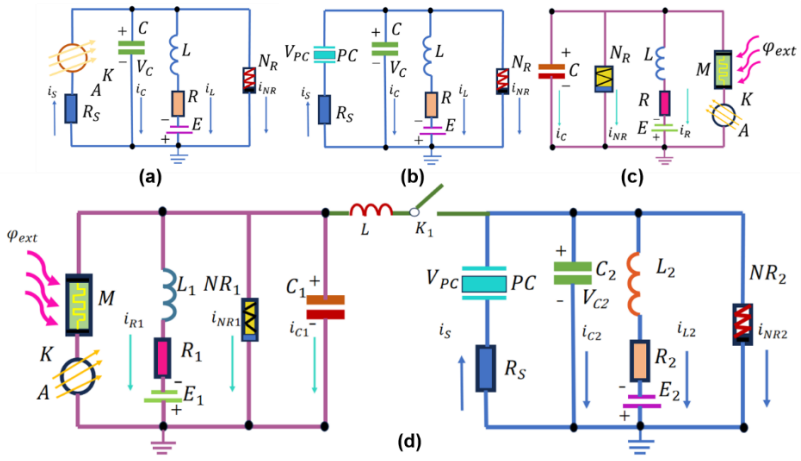

Figure 1. Schematic diagrams of neural circuit. (a) the isolated photosensitive neural circuit, (b) the isolated auditory neural circuit, (c) the novel photosensitive neuron incorporating a flux-controlled memristor, and (d) the functional neuron coupling mechanism.

i_{NR}, i_S, i_L and i_C denote the channel currents along the nonlinear resistor, the linear resistor, the induction coil L, and the capacitor C respectively.

V_S denotes the output voltage through the photocell, and C, L, R, R_S, E, and N_R denote capacitance, inductance, linear resistances, constant voltage source, and nonlinear resistance, respectively. According to Kirchhoff's law, the circuit equation of Figure 1(a) is given by

$$\begin{cases} C\dfrac{dV_C}{dt} = i_S - i_L - i_{NR}, \\ L\dfrac{di_L}{dt} = V_C - Ri_L + E. \end{cases} \tag{1}$$

Using $i_S = (V_S - V_C)/R_S$ to represent the photocurrent through the photocell, the voltage of the capacitor C is defined as V_C. In addition, the channel current through the nonlinear resistor NR is given by $i_{NR} = -\dfrac{1}{\rho}(V_C - \dfrac{V_C^3}{3V_0^2})$, where the parameters ρ and V_0 denote the resistance of the linear region and the cutoff voltage of the nonlinear resistor, respectively. The photocell acts as a voltage source V_S when a large resistance is applied in the resistor R_S, and the photocell can also act as a current source $i_S = \dfrac{2i_H}{\pi}\arctan(V_S - V_a)$ when a linear resistor R_S is selected in a finite resistance range.

Here, we mainly consider the case where the phototransistor is activated as a voltage source V_S and perform the standard scale transformation of the physical variables and parameters in equations as follows:

$$x_1 = \frac{V_C}{V_0}, y_1 = \frac{\rho i_L}{V_0}, \tau = \frac{t}{\rho C}, u_S = \frac{\rho}{R_S}\frac{V_S}{V_0}, \xi = \frac{\rho}{R_S},$$
$$a = \frac{E}{V_0}, b = \frac{R}{\rho}, c = \frac{\rho^2 C}{L}. \tag{2}$$

Thus, the dimensionless model equation for the photosensitive neuron can be expressed by

$$\begin{cases} \frac{dx_1}{d\tau} = x_1(1-\xi) - \frac{1}{3}x_1^3 - y_1 + u_S, \\ \frac{dy_1}{d\tau} = c(x_1 + a - by_1). \end{cases} \tag{3}$$

The variables x_1, y_1 and u_S represent membrane potential, slow current recovery variable, and external stimulus from the phototube, respectively. The phototube simulates the sensitivity of the retina to external light and incorporates the property of capturing specific bands of electromagnetic waves. During the dynamic simulation of neurons, only signals within a specific frequency range will be allowed to pass through the phototube, and signals outside the specific frequency range will be filtered because the amplitude has been altered and thus filtered. Furthermore, the exponential decay characteristic of phototubes stems from the equivalent behavior of their internal capacitance-resistance (RC) circuit. When an optical signal illuminates the cathode, electron emission generates a current. However, once the signal frequency exceeds the permissible passband range, the charge storage and release processes of the cathode material cause the output amplitude to decay exponentially. This behavior resembles the discharge curve of an RC circuit $V(t) = v_0 e^{-\tau/\lambda}$, where the time constant λ is determined by the electrical conductivity and dielectric constant of the cathode material.

The relationship between amplitude and frequency is as follows:

$$u_S = A_1(\omega_1, \tau)\cos(2\pi\omega_1\tau) \tag{4}$$

$$A_1(\omega_1, \tau) = \begin{cases} A_1 \exp(-\tau/\lambda_1), \omega_1 \geq \omega_{1\max}, \\ A_1, \omega_{1\min} \leq \omega_1 \leq \omega_{1\max}, \\ A_1 \exp(-\tau/\lambda_1), \omega_1 \leq \omega_{1\min}, \end{cases} \tag{5}$$

where the parameters ω_1 and A_1 control the main frequency and amplitude in the filtered waveform and voltage source, respectively. In addition, the normalization parameter λ_1 is usually considered an attenuation factor and is determined by the nature of the photocell cathode material. The attenuation factor λ_1, in physical terms, is related to the properties of the photocathode material. The parameter can be controlled by using different coating materials. The photocell will only allow certain light signals in a specific frequency band to pass through, thus absorbing and attenuating the energy of the photosensitive signal, and the higher value of the attenuation factor λ_1 means that external illumination can be quickly suppressed.

In addition, $\omega_{1\max}$ and $\omega_{1\min}$ define the upper and lower thresholds of the frequency filtering range, respectively, and it can be seen from the above equation that the external signal remains active in the region where the frequency belongs to [$\omega_{1\min}$, $\omega_{1\max}$], and the photocell is effectively activated. In the next section of a single-neuron system, we fix λ_1 = 5, [$\omega_{1\min}$, $\omega_{1\max}$] = [0.1,0.5].

On the other hand, realistic optical signals typically exhibit a broad frequency spectrum without special processing. Therefore, in experiments and studies, the output voltage of a chaotic circuit serves as an equivalent alternative. The output voltage of the Pikovski-Rabinovich (PR) is used as an optical signal, whose dynamics are described as

$$\begin{cases} \frac{dx'}{d\tau} = y' - \delta' z', \\ \frac{dy'}{d\tau} = -x' + 2\gamma y' + sz' + p, \\ \frac{dz'}{d\tau} = u(x' + z' - z'^3), \end{cases} \tag{6}$$

where the variables x', y', and z' can be mapped from the channel currents on the induction coil and the voltages on the capacitor in the chaotic circuit; the normalization parameters are: s = 0.165, p = 0.3, γ = 0.201, δ' = 0.66, and u = 1/0.047. In the next section, the initial values are fixed to (0.1,0.1,0.1), the chaotic sequences of the variables x' are used as the chaotic sequences of signals that are filtered by the optoelectronics and encoded by the external signal source, and this optical system is integrated into the neural coupling as an unfiltered chaotic optical signal.

2.2. Modeling of isolated auditory neurons

According to relevant studies, when a dielectric surface is subjected to acoustic waves and mechanical forces, it undergoes significant mechanical deformation. Concurrently, the distribution of the internal electric field is regulated by molecular polarity. As a result, transverse voltages are generated and altered in piezoelectric materials. Constant mechanical pressure produces a stable output voltage, whereas nonlinear vibrations induce time-varying voltages in piezoelectric devices. In Figure 1(b), the piezoelectric element is connected to a neural circuit that receives sound and processes the auditory signal. The principle behind this figure combines piezoelectric ceramic-coupled auditory neurons with an artificial neural circuit.

E, R_S, L, R, and N_R represent voltage sources, linear resistors, induction coils, constant voltage resistors, and nonlinear resistors, respectively, and the voltage of the capacitor describes the membrane potential of the neuron.

The physical relationship between the external pressure F and the voltage Vpc on the piezoelectric ceramic in Figure 1(b) can be expressed as

$$Vpc = V(F,p) = \frac{F}{S}\frac{d}{\varepsilon}h' = Pgh', P = \frac{F}{S}, g = \frac{d}{\varepsilon}, d = \frac{Q}{F}. \tag{7}$$

F, S, h', d, and ε are the mechanical external force, cross-sectional area, piezoelectric ceramic thickness, piezoelectric coefficient, and dependence on the physical properties of the material, respectively.

That is, the output voltage Vpc can estimate the effect of external vibrations and mechanical forces on this piezoelectric device. The current through the nonlinear resistor i_{NR} in Figure 1(b) can be estimated by

$$i_{NR} = -\frac{1}{\rho}(Vc - \frac{1}{3}\frac{V_C^3}{V_0}), \tag{8}$$

where the parameters ρ, V_0 and V_C denote the conductance, reverse voltage, and crossover

voltage of the nonlinear resistor, respectively. Based on the physical Kirchhoff's law, the circuit equation of the piezoelectric neuron circuit is given by

$$\begin{cases} C\dfrac{dVc}{d\tau} = \dfrac{Vpc - Vc}{Rs} - i_L - i_{NR}, \\ L\dfrac{di_L}{d\tau} = Vc - Ri_L + E. \end{cases} \tag{9}$$

Further, the physical variables and parameters in the above equation are mapped to dimensionless variables and normalized parameters by the following scale transformation:

$$\begin{aligned} &x_2 = \frac{Vc}{V_0}, y_2 = \frac{\rho i_L}{V_0}, \tau = \frac{t}{\rho C}, \xi = \frac{\rho}{Rs}, u_{PC} = \frac{V_{PC}}{V_0} \\ &a = \frac{E}{V_0}, b = \frac{R}{\rho}, c = \frac{\rho^2 C}{L}. \end{aligned} \tag{10}$$

Therefore, the dimensionless dynamics of the piezoelectric neuron are described by

$$\begin{cases} \dfrac{dx_2}{d\tau} = x_2(1-\xi) - \dfrac{1}{3}x_2^3 - y_2 + \xi u_{PC}, \\ \dfrac{dy_2}{d\tau} = c(x_2 + a - by_2). \end{cases} \tag{11}$$

From a kinetic point of view, the estimation and calculation of piezoelectric effects come mainly from the equivalent voltage-controlled currents u_{PC}, while the problem of possible mode selection in neural activity induced by external acoustic waves or mechanical forces can be well-solved by studying the sampling time series of membrane potentials x_2. Similar to the processing of phototubes for optical signals, acoustic waves are encoded by piezoelectric ceramics, and in practice, some bands in the acoustic waves can be quickly attenuated or completely absorbed by the medium. The mapped current can be described by signals of different angular frequencies as follows:

$$\xi u_{PC} = A_2(\omega_2, \tau)\cos\omega_2\tau + \zeta(\tau)\,. \tag{12}$$

The statistical relevance of estimating random perturbations $\zeta(\tau)$ here with Gaussian white noise with mean $\langle\zeta(\tau)\rangle=0$ is expressed as follows: For any noise intensity D, there holds $\langle\zeta(\tau)\ \zeta(\tau')\rangle=2\mathrm{D}\delta(\tau-\tau')$. Based on typical human daily environments, the signal-to-noise ratio (*SNR*) is set to *SNR* = 10, with the signal power in the system normalized to $S = 1$. According to the fundamental relationship for a signal-to-noise ratio, $D = S/SNR$, the noise intensity is consequently set to $D = 0.1$ in the following section.

The amplitude in the experimental sound signal actually depends on the angular frequency, and its correlation function is defined as

$$A_2(\omega_2, \tau) = \begin{cases} A_2\exp(-\tau/\lambda_2), \omega_2 \geq \omega_{2\max}, \\ A_2, \omega_{2\min} \leq \omega_2 \leq \omega_{2\max}, \\ A_2\exp(-\tau/\lambda_2), \omega_2 \leq \omega_{2\min}, \end{cases} \tag{13}$$

where A_2 is the amplitude of the current under piezoelectric action, and ω_2 is the angular frequency of the external sound signal. Similar to the attenuation factor λ_1, the attenuation factor λ_2 can be

determined by different piezoelectric materials. $\omega_{2\max}$ and $\omega_{2\min}$ define the upper and lower thresholds of the angular frequency filtering, respectively. In the next section of single neuron system, we fix the parameter $\lambda_2 = 5$, $[\omega_{2\min}, \omega_{2\max}] = [0.1,0.5]$.

Auditory signals in their raw state are often chaotic. In this study, the output voltage of a standard chaotic Chua circuit is employed to emulate such a signal. This approach allows for the adjustment and control of the effective angular frequency in the resulting stimulus current. The Chua oscillator is described by the following system of dynamical equations:

$$\begin{cases} \dfrac{dx''}{d\tau} = \eta(y'' - x'') - \eta f(x''), \\ \dfrac{dy''}{d\tau} = x'' - y'' + z'', \\ \dfrac{dz''}{d\tau} = -\psi y'' - \varpi z'', \end{cases} \tag{14}$$

where x'', y'', and z'' are dimensionless variables mapped from the output voltages of the two capacitors and the channel currents through the induction coil, and the normalization parameters η, ψ, ϖ are associated with the physical values of resistance, capacitance, and inductance. While the nonlinear function $f(x'')$ is

$$f(x'') = k_1 x'' + 0.5(k_0 - k_1)(|x''+1| - |x''-1|). \tag{15}$$

The parameters $\eta = 10$, $\psi = 16$, $\varpi = 0.01$, $k_0 = -1.296$, and $k_1 = -0.7364$ are set, and the initial values of the three variables are (0.01,0.1,1.0). In the next section, the sampled time series of variable x'' will be used as the unfiltered chaotic sound signal source.

2.3. A novel model of photosensitive neurons after the introduction of a memristor

As shown in Figure 1(a), the neural circuit of a single photosensitive neuron consists of three main components (*C*, *L*, and *NR*), as well as a phototube with a filtering effect, while the inflow and outflow of ions, as well as external stimuli, determine the complex activity of the neuron. The interaction of these factors leads to the induction of an electromagnetic field in the vicinity of the membrane, and a relationship can be established between the electromagnetic field and the ion flow. In this paper, a memristor (*M*) is introduced into the external stimulus branch so as to bridge the gap, as shown in Figure 1(c).

The equations in Figure 1(c) are as follows:

$$\begin{cases} C\dfrac{dV_C}{dt} = i_M - i_L - (-\dfrac{1}{\rho}(V_C - \dfrac{V_C^3}{3V_0^2})), \\ L\dfrac{di_L}{dt} = V_C + E + Ri_L, \\ \dfrac{d\varphi}{dt} = -u_1(V_C - V_S) - \varphi_{ext}, \end{cases} \tag{16}$$

where i_M is the current flowing through the memristor *M* and φ_{ext} represents the external magnetic flux, which is in the opposite direction of the electromagnetic field induced by the external stimulus

and membrane potential. For simplicity, the dimensionless representation φ_{ext} is expressed as $u_2\varphi'$. i_M is denoted as $i_M = U(\varphi)V_M = (\nu' + 3\sigma\varphi^2)(V_S - V_C)$.

Also, $U(\varphi) = \nu' + 3\sigma\varphi^2$ denotes the memductance of the memristor, ν' and σ are the relative parameters of the memristor, and φ denotes the magnetic flux. u_1 denotes the electromagnetic effect caused by the interaction of electrical stimulation and membrane potential. To normalize the relative parameters in the equations, the corresponding scale transformations are introduced as follows:

$$\alpha = \rho\nu', \beta = 3V_0^2C^2\rho^3\sigma, \varphi' = \frac{\varphi}{V_0\rho C}. \tag{17}$$

Then, the equations corresponding to the above three equations for the dimensionless dynamical system are updated as

$$\begin{cases} \dfrac{dx_1}{d\tau} = -(\alpha + \beta\varphi'^2)(x_1 - u_S) - y_1 + x_1 - \dfrac{1}{3}x_1^3, \\ \dfrac{dy_1}{d\tau} = c(x_1 + a - by_1), \\ \dfrac{d\varphi'}{d\tau} = -u_1(x_1 - us) - u_2\varphi'. \end{cases} \tag{18}$$

In this context, consistent with the photosensitive neuron described in the first subsection, the membrane potential and slow current recovery variable of the novel photosensitive neuron are still designated as x_1 and y_1. This nomenclature is maintained because subsequent comparative analysis of the discharge activities between the original and novel photosensitive neurons reveals that the x_1 and y_1 dynamics in the novel neuron exhibit enhanced synchronization properties, thereby facilitating more effective participation in coupling interactions. In the next section, we fix the parameters of Figure 1(d) to $u_1 = 1.0$, $u_2 = 5$, $\alpha = 0.01$, and $\beta = 0.03$, and we set the initial value to $\varphi'(0) = 0.1$.

2.4. Modeling the coupling of novel photosensitive neurons to auditory neurons

In this paper, we set up the photosensitive neuron model introducing a memristor to be coupled with the auditory neuron model for coil channel coupling, and the following kinetic equations of the coupled model in Figure 1(d) can be obtained:

$$\begin{cases} \dfrac{dx_1}{d\tau} = x_1 - \dfrac{1}{3}x_1^3 - y_1 - z - (\alpha + \beta\varphi'^2)(x_1 - u_S), \\ \dfrac{dy_1}{d\tau} = c(x_1 + a - by_1), \\ \dfrac{dx_2}{d\tau} = x_2(1 - \xi) - \dfrac{1}{3}x_2^3 - y_2 + + \xi u_{PC} + z, \\ \dfrac{dy_2}{d\tau} = c(x_2 + a - by_2), \\ \dfrac{dz}{d\tau} = K_1(\tau)(x_1 - x_2), \\ \dfrac{d\varphi'}{d\tau} = -u_1(x_1 - u_S) - u_2\varphi', \\ \dfrac{dK_1(\tau)}{d\tau} = \delta K_1(\tau)\upsilon(|\Delta H| - e). \end{cases} \tag{19}$$

Energy conservation in the system is associated with its vector fields. According to the Helmholtz theorem, a vector field can be decomposed into irrotational (gradient) and solenoidal (curl) components. This behavior aligns with the principles of the Helmholtz theorem, and the field energy accumulated within the neuronal circuit is quantified using the equivalent Hamilton energy. As a result, the intrinsic energy is stored in the capacitor, inductor, and memristor elements of novel photosensitive neurons.

Energy is usually defined as

$$E = \frac{1}{2}CV^2 + \frac{1}{2}Li_L^2 + \frac{1}{2}\int i_M d\varphi. \tag{20}$$

To derive the dimensionless Hamiltonian, and in conjunction with the points mentioned in the text, specifically, the memristor current $i_M = U(\varphi)V_M = (\nu + 3\sigma\varphi^2)(V_S - V_C)$, and apply scalar transformations of energy $H = E/CV_0^2$, we utilize the scale transformation from Eq (17) $\alpha = \rho\nu', \beta = 3V_0^2C^2\rho^3\sigma, \varphi' = \frac{\varphi}{V_0\rho C}$, then perform standard scaling using the following physical variables and parameters:

$$\begin{aligned} &x_1 = \frac{V_C}{V_0}, y_1 = \frac{\rho i_L}{V_0}, x_2 = \frac{Vc}{V_0}, \\ &y_2 = \frac{\rho i_L}{V_0}, u_S = \frac{\rho}{R_S}\frac{V_S}{V_0}, c = \frac{\rho^2 C}{L}, \\ &\alpha = \rho\nu', \ \ \beta = 3V_0^2C^2\rho^3\sigma, \varphi' = \frac{\varphi}{V_0\rho C}. \end{aligned} \tag{21}$$

Finally, the dimensionless Hamiltonian energy is obtained as

$$\begin{cases} H_1 = (\frac{1}{2}x_1^2 + \frac{1}{2c}y_1^2) - \frac{1}{2}(\alpha\varphi' + \beta\varphi'^3)\ (x_1 - us), \\ H_2 = \frac{1}{2}x_2^{2+}\frac{1}{2c}y_2^{\ 2}. \end{cases} \tag{22}$$

Therefore, in the coupling model of Figure 1(d), the criterion for the diversity of energy differences is:

$$\Delta H = H_1 - H_2 = (\frac{1}{2}x_1^2 + \frac{1}{2c}y_1^2) - \frac{1}{2}(\alpha\varphi' + \beta\varphi'^3)(x_1 - u_S) - (\frac{1}{2}x_2^2 + \frac{1}{2c}y_2^2). \tag{23}$$

It is proposed that $\frac{dK_1(\tau)}{d\tau} = \delta K_1(\tau)\upsilon(|\Delta H| - e)$ here to explore synaptic adaptivity and plasticity by developing criteria for synaptic activation and enhancement, i.e., an exponential increase in the strength of synaptic coupling when synaptic connections are enhanced to maintain field energy balance.

The gain δ represents the ratio of the increase in coupling strength of the coupled channel until an energy steady state gated by the Heaviside $\upsilon(*)$ function is reached, with a fixed value of $\delta = 0.001$. z is the current of the coil coupling channel, with the initial value set to $z = 0.001$. The initial value of the coupling strength $K_1(\tau)$ is set to $K_1(\tau) = 10^{-6}$, and further growth e is terminated when the energy difference falls below a threshold (which is set for simplicity). Therefore, the energy balance between two FHN neurons is fully controlled. In the coupling model, any differences in initial values, sound signals, or photocurrent between the two neurons will cause a significant disparity in Hamilton energy. This mismatch in neuronal parameters and excitability activates the synaptic connection,

causing the coupling strength to increase over time while the energy difference diminishes. Energy pumping and propagation continue until synchronization is achieved, thus fully controlling the energy balance between the two FHN neurons across the dual channels.

Over time, synaptic connections are aroused and strengthened in terms of coupling strength, and thus the energy difference diminishes until it stabilizes. In general, energy continues to be pumped and propagated until synchronization is reached. To obtain the time series $x(t) / x'(t)$, the Hilbert transform can be computed as follows:

$$\tilde{x}(t) = -\frac{1}{\pi} PV \int_{-\infty}^{+\infty} \frac{x(\tau)}{t-\tau} d\tau,\ \tilde{x}'(t) = -\frac{1}{\pi} PV \int_{-\infty}^{+\infty} \frac{x'(\tau)}{t-\tau} d\tau, \tag{24}$$

where *PV* represents the principal value of the integral and the phase steps are estimated as follows:

$$\hat{\phi}(t) = \arctan \frac{\tilde{x}(t)}{x(t)},\ \hat{\phi}'(t) = \arctan \frac{\tilde{x}'(t)}{x'(t)}. \tag{25}$$

Next, the degree of phase synchronization is measured by detecting the phase series in the variables $x(t)$ and $x'(t)$, calculating the phase error as follows:

$$\Delta\varphi = | p\hat{\phi}(t) - q\hat{\phi}'(t) | < \hat{\theta}, \tag{26}$$

where the values of the integers *p*, *q* can be completely determined when the size of the scale parameter $\hat{\theta}$ is set to 0.00001, so that the phase is locked at the *p*:*q* value when Eq (26) is completely satisfied.

Additionally, to assess whether the coupled model achieves complete synchronization, this paper adopts the criterion that complete synchronization between the two neurons is attained when the error $\Delta e < 10^3$. The error between the two neurons is defined as follows:

$$\triangle e = \sqrt{(x_1 - x_2)^2 + (y_1 - y_2)^2 + \varphi'^2}. \tag{27}$$

3. Numerical analysis and discussion

3.1. Isolated neuron model

In this section, the numerical solution of the neuronal model was solved using the fourth-order Runge-Kutta algorithm with a solution time step of h = 0.01, a transient period of about 3000 time units, and for a single neuron system, the parameters were fixed as a = 0.7, b = 0.8, c = 0.1, ξ = 0.175, and amplitudes of A_1 = 1, A_2 = 1.5 for Cases 1 to 5. The initial values of the membrane potentials of the two neurons were set to [x_1, y_1] = [0.1,0.1], and [x_2, y_2] = [0.1,0.3], respectively.

3.1.1. Modeling of isolated photosensitive neurons

In Figures 2 and 3, the dynamic analysis of isolated light-dependent circuits as well as isolated acoustic-signal-dependent circuits was estimated by calculating the maximal Lyapunov exponent, the bifurcation analysis, and the phase portrait of isolated photosensitive neurons and isolated auditory neurons, respectively.

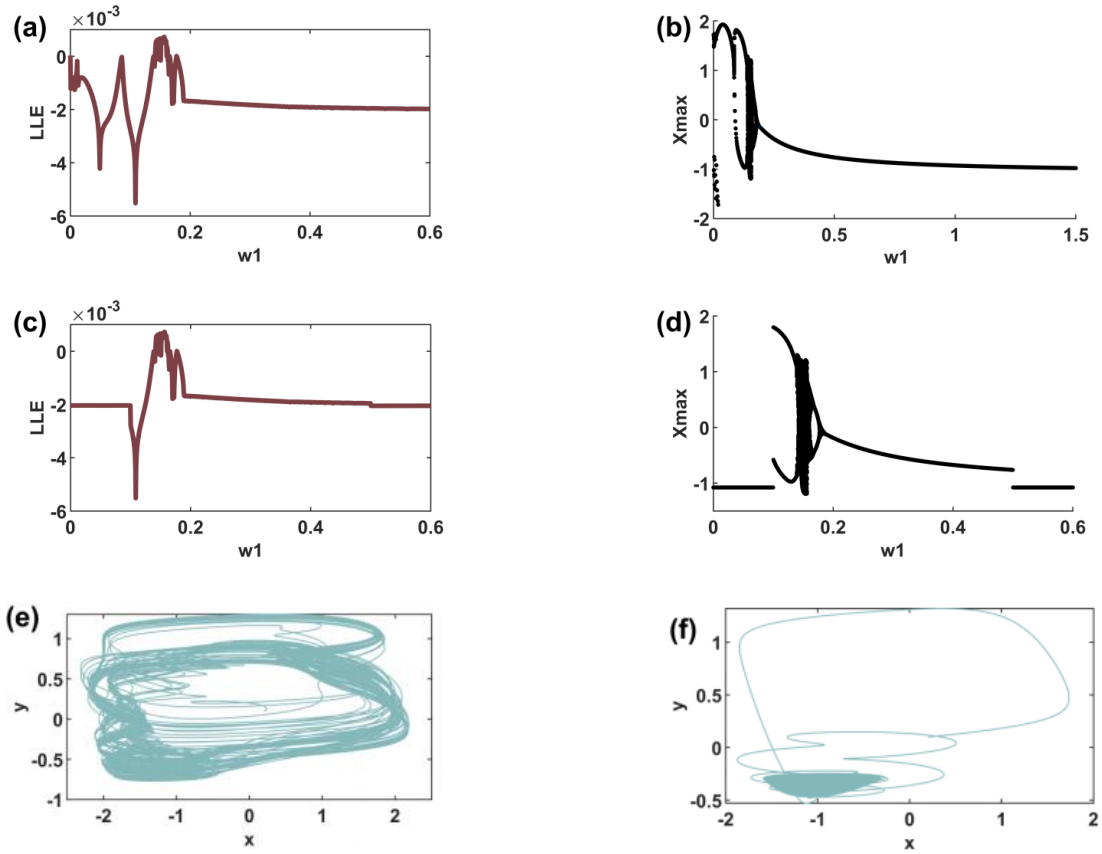

Figure 2. Dynamic display of an isolated photosensitive neuron. (a) and (c) maximum Lyapunov exponent; (b) and (d) bifurcation analysis of the membrane potential; (e) and (f) phase portrait of the isolated photosensitive neuron, where the external stimulus in (a), (c), and (e) are chaotic signals, and the external stimulus in (b), (d), and (f) are filtered voltage sources. The attenuation factor is λ_1 =15.

From the membrane potential sequence plots in Figures 2(a),(c), or the bifurcation plots in Figures 2(b),(d), it can be seen that the isolated photosensitive neurons are in a periodic discharge state at $w_1 < 0.14$ and in a chaotic state in the range of $w_1 \in (0.14, 0.17)$. Signals with frequencies outside of [0.1,0.5] are progressively filtered, and the corresponding bifurcation maps are correspondingly segmented. Correspondingly, the phase portraits in Figures 2(e),(f) show a chaotic attractor under chaotic signal stimulation and a limit cycle (periodic attractor) when a filtered signal is applied.

3.1.2. Modeling of isolated auditory neurons

In Figure 3, the maximal Lyapunov exponent plots in Figures 3(b),(d) indicate periodic firing under both signal conditions. However, the bifurcation diagrams in Figures 3(a),(c) reveal distinct patterns, highlighting the differential effect of the filtering process. The phase portrait in Figure 3(e) under chaotic signal stimulation is chaotic, while the phase portrait in Figure 3(f), after effective filtering by piezoelectric ceramics, ends up in a periodic state.

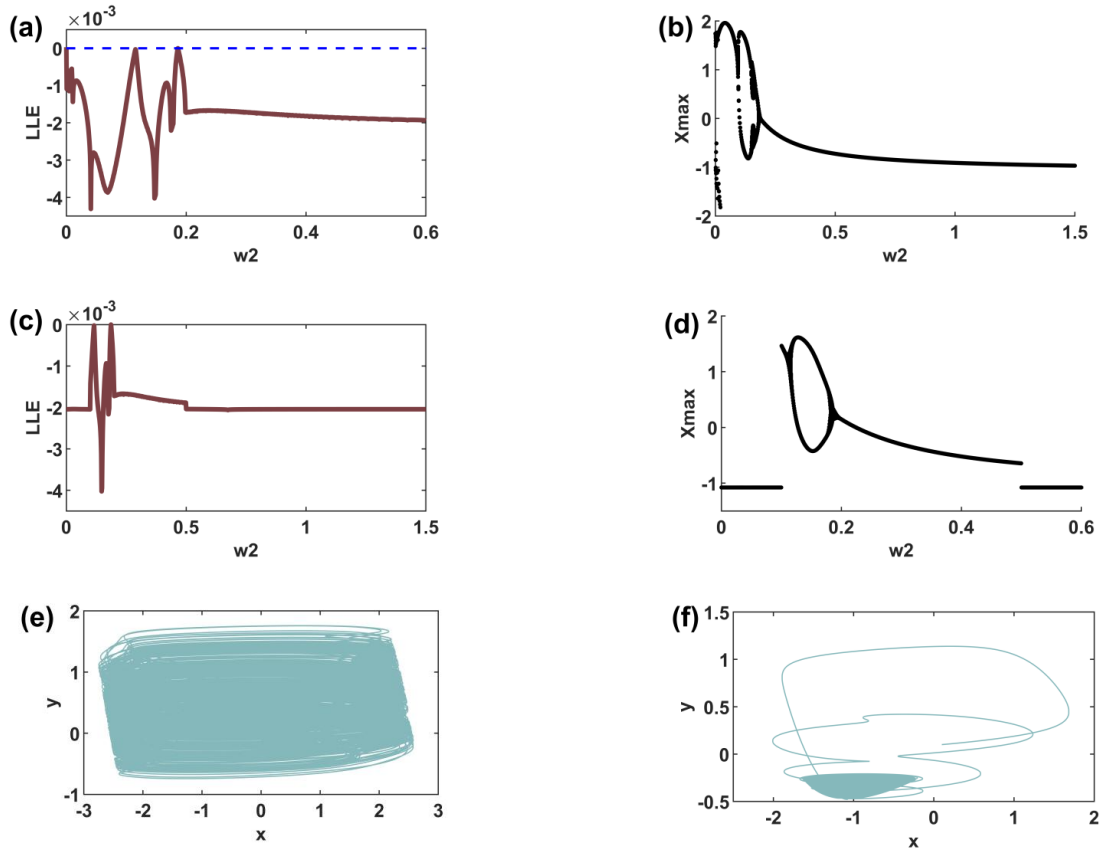

Figure 3. Dynamic display of an isolated auditory neuron. (a) and (c) maximum Lyapunov exponent map versus voltage source frequency; (b) and (d) bifurcation analysis of the membrane potential of the isolated neuron in response to an external stimulus; and (e) and (f) display the phase portrait of the isolated auditory neuron, where the external stimulus in (a), (c), and (e) is the chaotic signal, and the external stimulus in (b), (d), and (f) is the filtered signal. The attenuation factor is $\lambda_2 = 15$.

3.1.3. Modeling of isolated novel photosensitive neurons

As can be seen in Figure 4, unlike the previous photosensitive neuron, the maximum Lyapunov exponent plots in Figures 4(a),(c) of the novel photosensitive neuron under different filtering conditions are overall negative, corresponding to the state of periodic firing in the bifurcation plots Figures 4(b),(d). Under the stimulation of chaotic signals, the degree of chaos in the phase portrait in Figures 4(e) is weakened compared to the original photosensitive neuron, and the phase portrait in Figure 4(f) enters the periodic state more quickly under the same filtering signal. The results indicate that the novel photosensitive neuron has a more regular firing activity. Compared to conventional photosensitive neurons without memristors, the nonvolatile nature of memristors enables memristive photosensitive neurons to respond to current stimuli, such as whether to discharge based not only on the present stimulus intensity but also on the historical stimulus trajectory. Furthermore, under filtered external signal stimulation, they enter periodic states more rapidly. This facilitates the exploration of synchronous dynamic behaviors in more favorably coupled multi-neuron networks. Therefore, in the following section, the novel photosensitive neuron is coupled with the auditory neuron for further study.

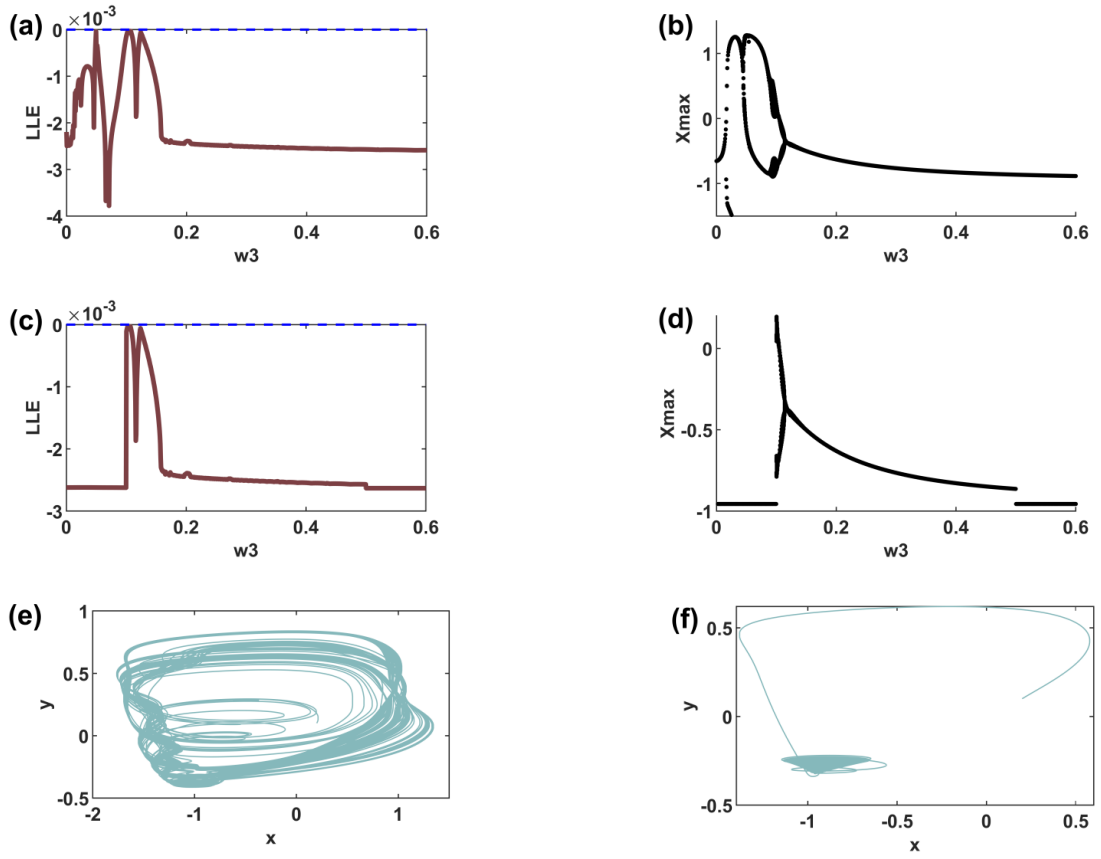

Figure 4. Dynamic display of a novel isolated photosensitive neuron. (a) and (c) maximum Lyapunov exponent map versus voltage source frequency; (b) and (d) bifurcation analysis of the membrane potential of the isolated neuron in response to an external stimulus; and (e) and (f) display the phase portrait of the isolated photosensitive neuron, where the external stimulus in (a), (c), and (e) is the chaotic signal, and the external stimulus in (b), (d), and (f) is the filtered signal. The attenuation factor is $\lambda_1 = 15$.

3.2. Coupling of novel photosensitive neurons with auditory neurons

Sensory neurons in organisms (whether photoreceptive or auditory) typically exhibit frequency selectivity. Their response to external stimuli is not indiscriminate; instead, they are particularly sensitive to signals within specific frequency bands. Wave filtering light and sound signals essentially extract the frequency components within each modality that most effectively drive neuronal discharge. This process filters out noise and irrelevant frequency components (too high or too low) that do not match neuronal responses. Consequently, it enables faster establishment of regular discharge activity from random noise, laying the foundation for synchronization. Therefore, in the experimental design described below, filtered signals are still selected as external stimuli.

We consider five coupling scenarios, all analyzed dynamically using the model shown in Figure 1(d). For simplicity, the auditory neuron and novel photosensitive neuron are denoted as ADN and NLDN, respectively. All neurons are stimulated by a linearly swept chirp signal. Based on the filtering mechanism, the sweeping optical and acoustic signals are updated as follows.

It is discussed below in five scenarios:

Case 1. The NLDN and ADN are coupled under excitation by unfiltered external signals, with identical parameters but different initial values.

Case 2. The NLDN is excited by an unfiltered external signal, while the ADN is excited by a band-pass filtered swept-frequency chirp signal (center frequency w_2, bandwidth BW_2). The system has identical parameters, different initial values, and a filter attenuation factor $\lambda_2 = 15$.

Case 3. The NLDN is excited by a band-pass filtered swept-frequency chirp signal (center frequency w_1, bandwidth BW_1), while the ADN is excited by an unfiltered external signal. The system has identical parameters, different initial values, and a filter attenuation factor $\lambda_1 = 15$.

Case 4. Dual-mode swept-frequency filtered excitation: The NLDN and ADN receive band-pass filtered swept-frequency chirp signals (center frequencies w_1 and w_2; bandwidths BW_1 and BW_2, respectively), with identical parameters, different initial values, and filter attenuation factors $\lambda_1 = \lambda_2 = 15$.

Case 5. Dual-mode swept-frequency filtered excitation: The NLDN and ADN receive band-pass filtered swept-frequency chirp signals, with different parameters, identical initial values, and filter attenuation factors $\lambda_1 = \lambda_2 = 15$.

The other fixed parameters are: $\xi = 0.5$, $a = 0.7$, $b = 0.8$, $c = 0.1$.

Additionally, based on the filtering of external signals, this subsection further employs a linear chirp signal as the final external excitation source, whose instantaneous frequency varies linearly with time. The mathematical expression of the linear chirp signal is

$$\begin{cases} w(t) = w_0 + \triangle wt, \\ \bar{\phi}(t) = 2\pi(w_0 t + \triangle wt^2 / 2), \\ S(t) = A\cos[\bar{\phi}(t)], \end{cases} \tag{28}$$

where w_0 is the initial frequency, $\triangle w$ is the difference between the final and starting frequencies, $\bar{\phi}$ is the accumulated phase, and $S(t)$ is the chirp signal. Consequently, after incorporating the signal filtering settings from Eqs (5) and (13), the optical and auditory signals are modified as follows:

$$\begin{aligned} u_S &= A_1(\omega_1, \tau)\cos(2\pi\tilde{\omega}_1\tau + \omega_1\tau^2 / 2), \\ \xi u_{PC} &= A_2(\omega_2, \tau)\cos(\tilde{\omega}_2\tau + \omega_2\tau^2 / 2) + \zeta(\tau), \end{aligned} \tag{29}$$

where $\tilde{\omega}_1$ and $\tilde{\omega}_2$ represent the initial frequencies of the respective signals.

In the numerical implementation, continuous signals are approximated through discrete-time sampling with a solution time step of $h = 0.01$ and a total of $N = 3000$ sampling points, ensuring sufficient frequency resolution.

In this study, Gaussian white noise was added to both external stimulus signals to simulate the high-noise environment commonly encountered in in vivo recordings, thereby testing the robustness of the model's coupling synchronization mechanism under adverse conditions. To highlight the key findings, the graphical presentation in this section focuses on variables that significantly influence synchronization behavior. In Cases 1 and 3, the inherently chaotic nature of the unfiltered optical or auditory signals (Figures 5 and 6) prevents the system from achieving synchronization; consequently, additional noise perturbations do not alter this non-synchronized state. Furthermore, in Cases 2 and 4, our tests and quantitative analysis confirmed that the impact of adding noise to the optical signal is negligible on the synchronization outcome. Thus, to avoid redundancy and ensure clarity, only the critical comparison filtered auditory signals versus without added noise, is presented in the main text. Complete datasets are available upon request.

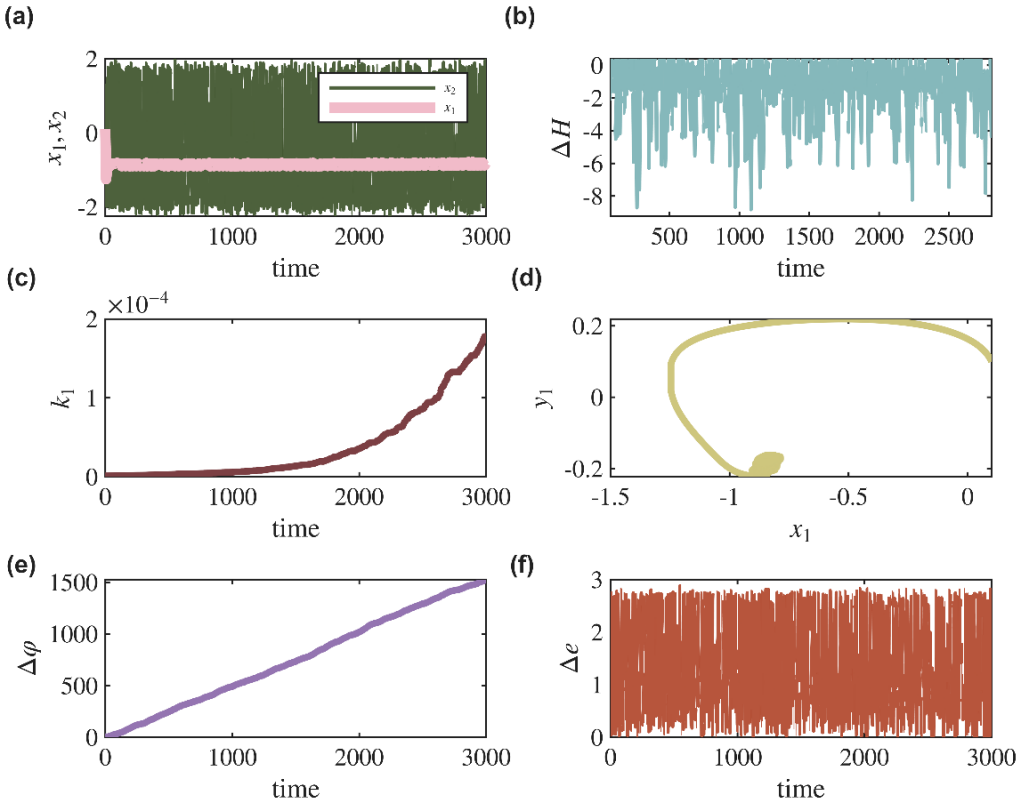

Figure 5. Sampling time series of Case 1. (a) membrane potential time series, (b) Hamilton energy difference, (c) coil coupling strength, (d) attractor of the photosensitive neuron, (e) phase difference, and (f) coupling error.

Subplot labels with a subscript 1 indicate coupling involving noise-free auditory signals, while those with a subscript 2 indicate coupling involving auditory signals with added noise.

In Case 1, two differently functioning neurons under light and acoustic stimulation are connected by an inductive coil, and both sides receive either light or sound signals as chaotic signals, after which the coupling strength is controlled and increased according to a defined criterion. That is, the energy diversity between the neurons makes the synaptic connections stronger with increasing strength, and the results for Case 1 are shown in Figure 5.

In Figure 5, the coupling strength corresponding to the Figure 5(c) plot shows an exponential increase in the coupling strength, and the activation of the coupled channel is dependent on the release of neurotransmitters, which enhances the self-adaptation of the neural system. The NLDN and ADN differ in that they have different parameters and receive very different external stimuli, and thus even though the coupling strength increases greatly, the Hamiltonian energy difference shown in Figure 5(b) as well as the coupling error in Figure 5(f) cannot be reduced to a certain threshold, so the membrane potential map in Figure 5(a), the phase attractor in Figure 5(d), and the phase difference map in Figure 5(e) cannot be fully synchronized.

In Case 2, the auditory signal is effectively filtered. As shown in Figure 7, the membrane potential in Figure 7(a1), energy difference in Figure 7(b1), and coupling error in Figure 7(f1) of the auditory neuron all decrease in the latter phase, coinciding with the system's convergence to a synchronous attractor shown in Figure 7(d1). The phase difference map in Figure 7(e1) can also be synchronized

through parameter adjustment. However, the system fails to achieve complete synchronization, as evidenced by the coupling strength that increases exponentially over time (Figure 7(c1)) and a persistently positive maximum Lyapunov exponent (Figure 7(g1)). This indicates that filtering only one signal is insufficient for robust synchronization. The introduction of noise to the auditory signal further disrupts the filtering effect and these partial synchronous states, as evidenced by the results shown in Figures 7(a2),(b2),(c2),(d2),(e2),(f2),(g2).

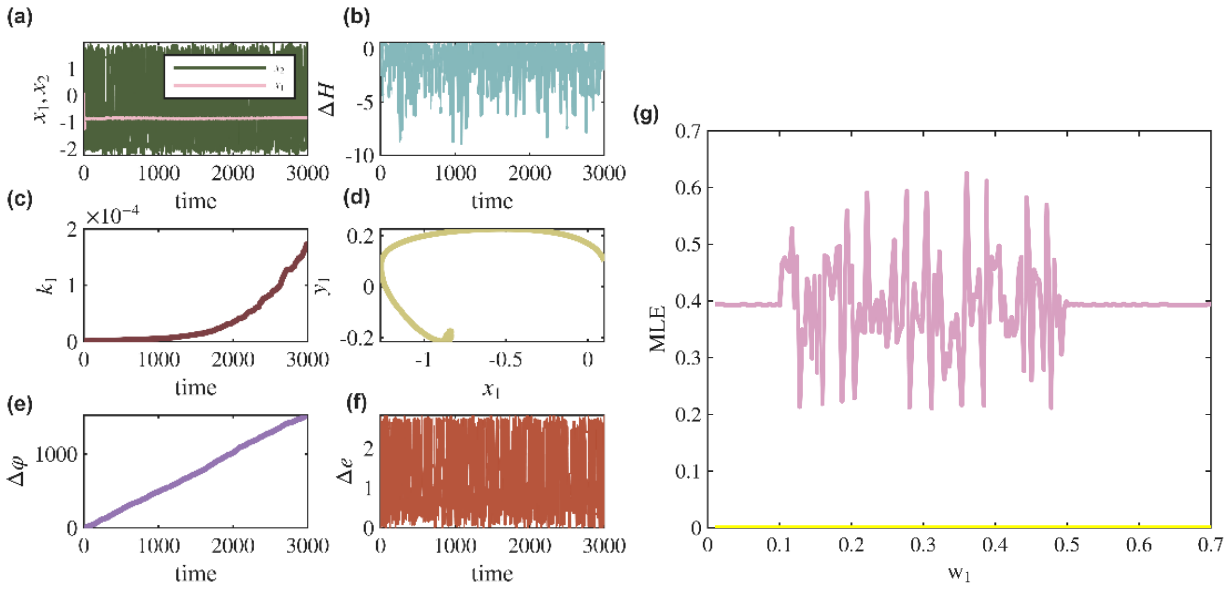

Figure 6. Sampling time series of Case 3. (a) membrane potential time series, (b) Hamilton energy difference, (c) coil coupling strength, (d) attractor of the photosensitive neuron, (e) phase difference, (f) coupling error, and (g) maximum Lyapunov exponent.

It can be observed from Figures 6(a)–(g) that the two neuron couplings ultimately fail to synchronize under the premise that only the light signal is effectively filtered while the sound signal remains chaotic.

In Case 4, with simultaneous input of filtered optical signals (with noise) and auditory signals (without noise), the coupled system achieves synchronization. As shown in Figure 8, as the gain increases, the Hamiltonian energy difference shown in Figure 8(b1) reaches quasi-equilibrium, the coupling error shown in Figure 8(f1) converges to zero, the coil coupling strength shown in Figure 8(c1) and the phase difference in Figure 8(e1) stabilize, resulting in synchronized membrane potential sequences as shown in Figure 8(a1) and a coherent attractor shown in Figure 8(d1). The maximum Lyapunov exponent (Figure 8(g1)) further confirms the synchronization interval. However, when noise is introduced to the auditory signal, multiple synchronization indicators are disrupted in Figures 8(a2),(b2),(c2),(d2),(e2),(f2),(g2). Indeed, biological sensory neurons, whether photic or auditory, inherently exhibit frequency selectivity. Their response to external stimuli is not indiscriminate but is preferentially tuned to specific frequency bands. Applying band-pass filtering to optical and acoustic signals essentially extracts the characteristic frequency components within each sensory modality that are most efficacious in evoking neuronal spiking. This process attenuates noise and irrelevant spectral components (both higher and lower frequencies) that are suboptimal for driving the neuronal response. Consequently, this allows the system to establish

regular, stimulus-locked firing patterns more rapidly from a stochastic background, thereby laying a functional foundation for the emergence and maintenance of neuronal synchronization. These results demonstrate that the coupled system exhibits asymmetric robustness to bimodal input noise: It remains insensitive to optical channel noise, yet its synchronization stability critically depends on the purity of the auditory signal.

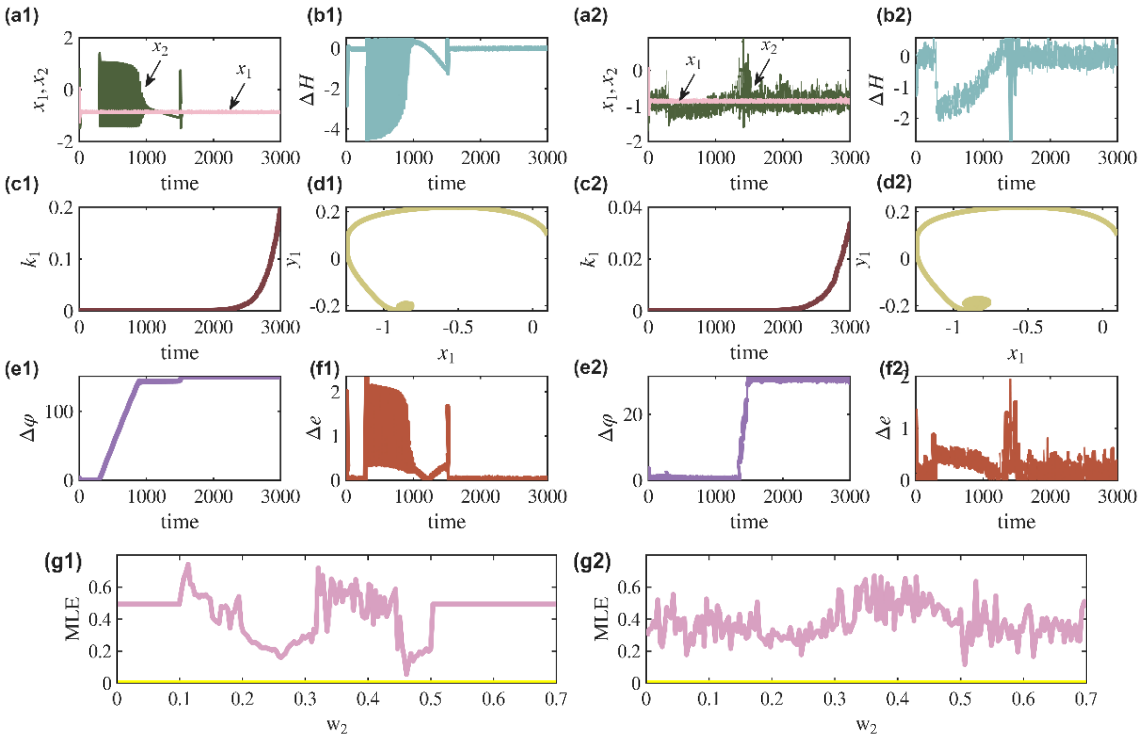

Figure 7. Sampling time series of Case 2. (a1) and (a2) membrane potential time series, (b1) and (b2) Hamilton energy difference, (c1) and (c2) coil coupling strength, (d1) and (d2) attractor the of photosensitive neuron, (e1) and (e2) phase difference, (f1) and (f2) coupling error, and (g1) and (g2) maximum Lyapunov exponent.

Figures 8(g1),(g2) present heatmaps depicting the distribution of the maximal Lyapunov exponent of the coupled system as a function of parameters ω_1 and ω_2. In Figures 8(g1),(g2), the color gradient from blue to red corresponds to the value of the maximal Lyapunov exponent, ranging from negative to positive. According to the color bar: Warm-colored regions (red/yellow) indicate a positive exponent, signifying a chaotic state; cool-colored regions (light blue/deep blue) indicate a negative exponent, meaning the system is in a periodic or synchronous state; and green regions indicate an exponent near zero, corresponding to the system being at the edge of chaos or a bifurcation point.

Figure 8(g1) demonstrates that even with the implementation of dual filtering, the parameter regions conducive to synchronization remain limited. In contrast, the scattered distribution of synchronized parameter points in Figure 8(g2) indicates that the introduction of noise does not completely disrupt synchronization, as the system can still attain a synchronized state for specific parameter configurations. These findings collectively reveal that the coupled system exhibits an asymmetric robustness to bimodal input noise: It is largely insensitive to noise in the visual channel, yet the stability of synchronization is critically dependent on the signal purity of the auditory pathway.

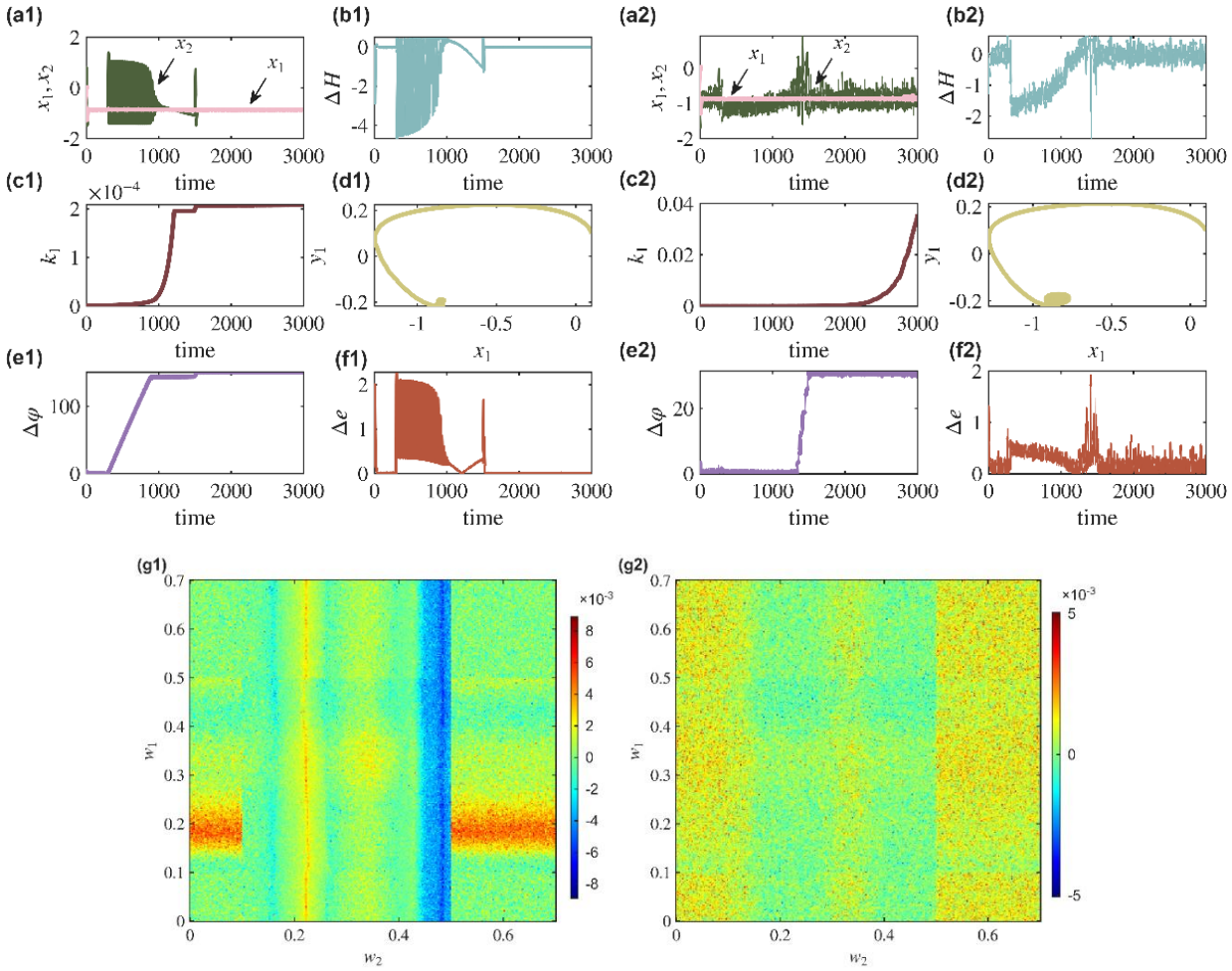

Figure 8. Sampling time series of Case 4. (a1) and (a2) membrane potential time series, (b1) and (b2) Hamilton energy difference, (c1) and (c2) coil coupling strength, (d1) and (d2) attractor photosensitive neuron, (e1) and (e2) phase difference, (f1) and (f2) coupling error, and (g1) and (g2) maximum Lyapunov exponent.

In Case 4, with identical parameters and different initial values, the system can achieve synchronization under altered parameter configurations, see Figures 9(a1),(b1),(c1),(d1),(e1),(f1),(g1), exhibiting synchronous states distinct from those in Figure 8. This reflects the rich dynamic repertoire of the coupled system. Similarly, as shown in Figures 9(a2),(b2),(c2),(d2),(e2),(f2),(g2), introducing noise to the auditory signal disrupts synchronization.

Figures 9(g1),(g2) present heatmaps depicting the distribution of the maximal Lyapunov exponent of the coupled system as a function of parameters ω_1 and ω_2. In Figures 9(g1),(g2), the color gradient from blue to red corresponds to the value of the maximal Lyapunov exponent, ranging from negative to positive. According to the color bar: Warm-colored regions (red or yellow) indicate a positive exponent, signifying a chaotic state; cool-colored regions (light blue or deep blue) indicate a negative exponent, meaning the system is in a periodic or synchronous state; and green regions indicate an exponent near zero, corresponding to the system being at the edge of chaos or a bifurcation point.

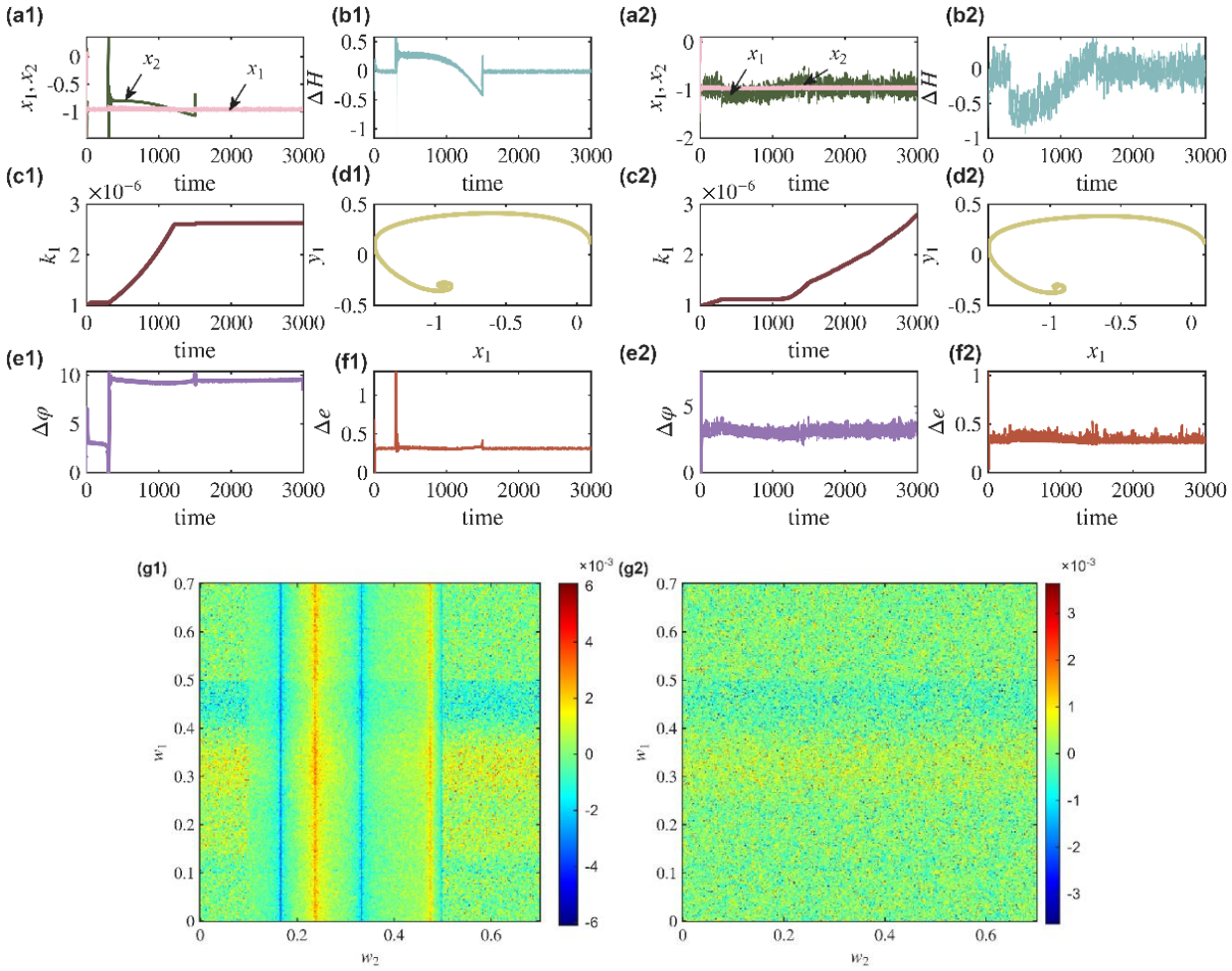

Figure 9. Sampling time series of Case 4. (a1) and (a2) membrane potential time series, (b1) and (b2) Hamilton energy difference, (c1) and (c2) coil coupling strength, (d1) and (d2) attractor of the photosensitive neuron, (e1) and (e2) phase difference, (f1) and (f2) coupling error, and (g1) and (g2) maximum Lyapunov exponent.

Figures 9(g1),(g2) reveal a notable phenomenon within specific, localized parameter regions: The coupled system fails to achieve synchronization when the auditory signal is noise-free, yet the introduction of noise actively promotes the emergence of synchronization. This indicates that the influence of noise on system synchronization is not universally detrimental; under certain parametric conditions, mechanisms such as stochastic resonance or noise-induced phase transitions can enhance synchronization capability. These results underscore the dual role of noise in nonlinear dynamics: It is capable of both disrupting established synchronization and, in weakly synchronized regimes, optimizing the system's response. This further highlights the inherent complexity and adaptive nature of multisensory integration processes. Although the primary objective of this study was to validate the efficacy of bimodal filtering, and a systematic scan of noise intensity was not performed, the dual role of noise in nonlinear dynamics where it can either disrupt synchronization or, conversely, enhance it through mechanisms such as stochastic resonance, has been theoretically and experimentally supported in multiple studies [32–34]. This class of phenomena warrants further investigation in future work, combining systematic noise intensity scans with in-depth theoretical analysis. Here, the parameters in Figure 9 are set to $\xi = 0.36$, $a = 0.8$, $b = 0.5$, and $c = 0.3$; the initial values of the membrane

potentials of the two neurons are set to $[x_1, y_1] = [0.1,0.1]$, and $[x_2, y_2] = [0.1,0.3]$.

As shown in Figures 10(a1),(b1),(c1),(d1),(e1),(f1), parameter mismatch between the two neurons impedes the achievement of synchronization in the coupled system. Correspondingly, Figures 10(a2),(b2),(c2),(d2),(e2),(f2) demonstrate that introducing noise into the auditory input further exacerbates the system's chaotic dynamics. This observation is supported by prior studies [35], which indicate that parameter mismatch induces a disparity in the intrinsic firing frequencies of neurons, thereby impeding synchronization under conditions of weak or absent coupling. Even when coupling is present, a significant mismatch can render the coupling strength insufficient to overcome the inherent frequency difference, thus obstructing synchronization. Consequently, the phenomenon observed in this study, where noise input exacerbates chaos in a system already predisposed to instability by parameter mismatch, is consistent with established theoretical principles. The parameters in Figure 10 are set to $\xi = 0.85$, $a = 0.7$, $b = 0.95$, and $c = 0.1$ for the novel photosensitive neuron, and set to $\xi = 0.69$, $a = 0.3$, $b = 1$, and $c = 0.4$ for the auditory neuron. The initial values of the membrane potentials of the two neurons are set to $[x_1, y_1] = [0.1,0.1]$, and $[x_2, y_2] = [0.1,0.1]$.

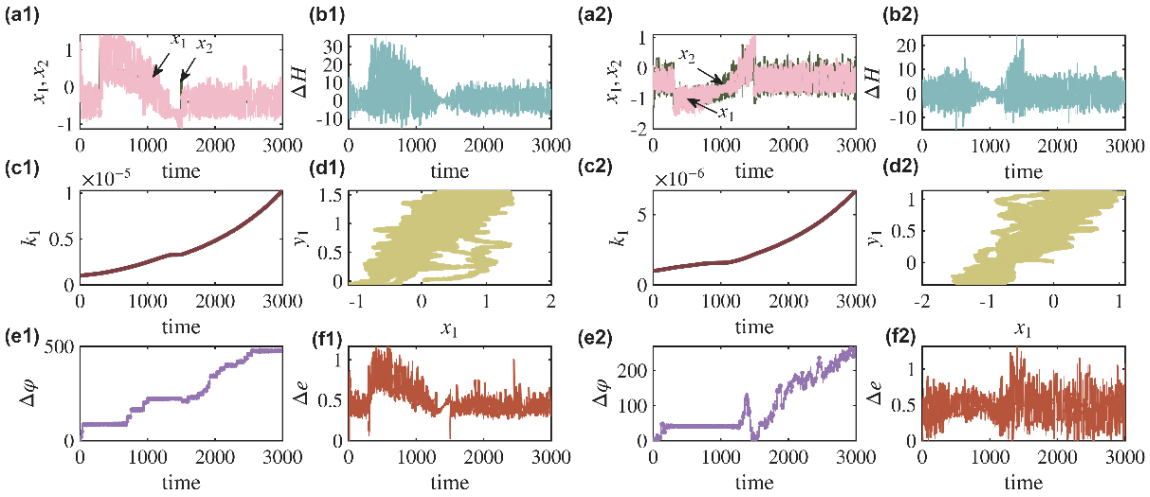

Figure 10. Case 5 sampling time series. (a1) and (a2) membrane potential time series, (b1) and (b2) Hamilton energy difference, (c1) and (c2) coil coupling strength, (d1) and d2) attractor of the photosensitive neuron, (e1) and (e2) phase difference, and (f1) and (f2) coupling error.

3.3. Effect of parameter variation on model coupling

From the graphical results of Cases 4 and 5 in Section 3.2, the following discussions all presuppose that the two functional neurons have the same parameters.

Figure 11 illustrates synchronization dynamics under different conditions. Figures 11(a),(b) depict the system's behavior under ideal noise-free inputs for both optical and auditory signals. In contrast, Figures 11(c),(d) show the response under adverse conditions with noise introduced solely into the auditory pathway. The comparison highlights the critical impact of auditory noise on synchronization, demonstrating that it significantly alters parameter regions conducive to synchronization and reveals a specific vulnerability to auditory perturbations. This asymmetric robustness is consistent with time-series analysis findings.

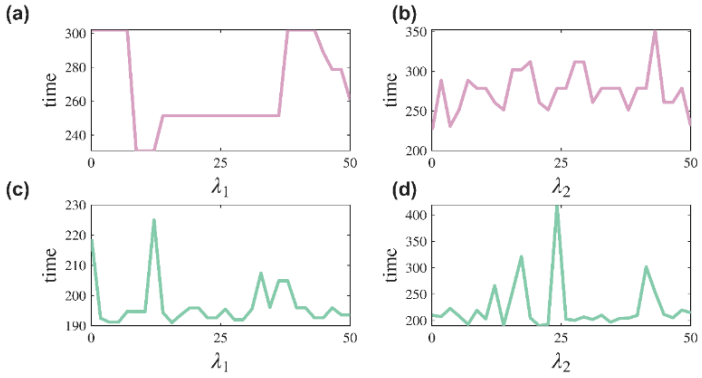

Figure 11. Coupled synchronization time series plot for fixing one parameter to transform the other, i.e., fixing $\lambda_1 = 15$ and $\lambda_2 = 15$, respectively. Subplots (a) and (b) show auditory signals without noise; (c) and (d) show auditory signals with added Gaussian white noise.

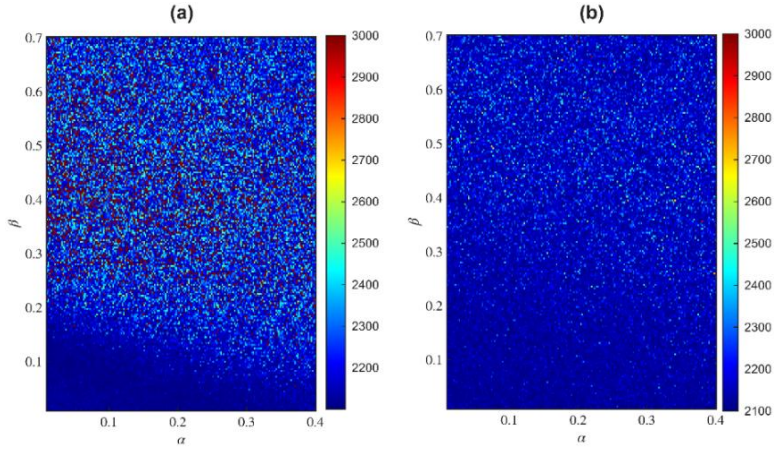

Figure 12. Heatmap of the synchronization time in the flux parameter $\alpha - \beta$ space of the memristor. (a) corresponds to the coupled system with a noise-free auditory signal, while (b) corresponds to the system with Gaussian white noise added to the auditory signal. The color bar represents the synchronization time, where lower values indicate that the coupled system achieves the synchronized state more rapidly.

The results in Figure 11 demonstrate that the introduction of noise into the auditory signal significantly compresses the parameter space within which the system can maintain synchronization, thereby increasing the difficulty of achieving synchronized states. However, as observable in Figures. 12(a),(b), this configuration does not entirely eliminate the possibility of synchronization. Under specific, albeit sparse, parameter configurations, the system not only achieves synchronization but can do so with potentially accelerated dynamics. This evidence indicates that while the auditory pathway exhibits vulnerability to noise interference, it concurrently demonstrates a degree of adaptability and complexity in its neural dynamics.

4. Conclusions

This study investigates the influence of effectively filtered external signals on the synchronization of coupled functional neurons. It begins by introducing models of photosensitive neurons, auditory

neurons, and a novel magnetically controlled memristive photosensitive neuron, along with an analysis of the chaotic nature of external signals and the filtering methods employed. Through inductive coupling, the memristor-based photosensitive neuron is coupled with the auditory neuron. The effects of different filtering combinations, parameters, and initial conditions on synchronization performance are compared. Under dual-filtering conditions, the regulation of synchronization time intervals by varying attenuation factors, magnetic flux-related parameters, and the amplitude and frequency of the filtered signals is explored.

The main findings are as follows:

1) The introduction of a memristor enhances the dynamical stability of the photosensitive neuron, where the interaction between membrane potential and electromagnetic field maintains regular spiking oscillations.

2) Dual-filtering facilitates neuronal synchronization, whereas synchronization is difficult to achieve when at least one of the signals is chaotic.

3) The coupling system exhibits nonlinearity due to the memristor and inductive pathway, but shorter synchronization time windows can be identified by adjusting attenuation factors, signal amplitude and frequency, and magnetic flux-related parameters.

4) Under certain conditions, using non-identical parameters may result in smaller phase differences, which could be beneficial for parameter optimization.

Furthermore, the resting-state synchronization achieved in this study not only possesses mathematical stability but also reflects a foundational level of system integration. It establishes a theoretical basis for coordinated responses in cross-modal neural prostheses (e.g., light-sound combined implantable devices) under low-power standby conditions and provides a computational model for understanding the ground-state dynamics of multisensory integration in the brain.

Use of AI tools declaration

The authors declare they have not used Artificial Intelligence (AI) tools in the creation of this article.

Acknowledgments

This research has been conducted with the support of the National Natural Science Foundation of China (Nos. 12172210 and 11502139).

Conflict of interest

The authors declare there is no conflict of interest.

References

1. D. Hansel, G. Mato, C. Meunier, Phase dynamics for weakly coupled Hodgkin-Huxley neurons, *Europhys. Lett.*, **23** (1993), 367–372. https://doi.org/10.1209/0295-5075/23/5/011
2. Y. Wang, D. T. W. Chik, Z. D. Wang, Coherence resonance and noise-induced synchronization in globally coupled Hodgkin-Huxley neurons, *Phys. Rev. E*, **61** (2000), 740–746. https://doi.org/10.1103/PhysRevE.61.740

3. S. Lee, S. Kim, Parameter dependence of stochastic resonance in the stochastic Hodgkin-Huxley neuron, *Phys. Rev. E*, **60** (1999), 826–830. https://doi.org/10.1103/PhysRevE.60.826
4. F. G. C. Cabarle, Thinking about spiking neural P systems: Some theories, tools, and research topics, *J. Membr. Comput*., **6** (2024), 148–167. https://doi.org/10.1007/s41965-024-00147-y
5. P. Pietrzak, S. Szczęsny, D. Huderek, Ł. Przyborowski, Overview of spiking neural network learning approaches and their computational complexities, *Sensors*, **23** (2023), 3037. https://doi.org/10.3390/s23063037
6. S. Yang, D. Li, J. Feng, B. Gong, Q. Song, Y. Wang, et al., Secondary order RC sensor neuron circuit for direct input encoding in spiking neural network, *Adv. Electron. Mater*., **10** (2024), 2400075. https://doi.org/10.1002/aelm.202400075
7. Q. Xu, X. Chen, B. Chen, H. Wu, Z. Li, H. Bao, Dynamical analysis of an improved FitzHugh-Nagumo neuron model with multiplier-free implementation, *Nonlinear Dyn*., **111** (2023), 8737–8749. https://doi.org/10.1007/s11071-023-08274-4
8. X. Zhang, F. Min, Y. Dou, Y. Xu, Bifurcation analysis of a modified FitzHugh-Nagumo neuron with electric field, *Chaos Solitons Fractals*, **170** (2023), 113415. https://doi.org/10.1016/j.chaos.2023.113415
9. S. Zhou, G. Huang, R. Zhu, Y. Wang, Y. Chai, Research on the synchronization of a controllable memristive photosensitive FitHugh-Nagumo model, *Opt. Laser Technol*., **175** (2024), 110736. https://doi.org/10.1016/j.optlastec.2024.110736
10. F. Yang, J. Ma, A controllable photosensitive neuron model and its application, *Opt. Laser Technol*., **163** (2023), 109335. https://doi.org/10.1016/j.optlastec.2023.109335
11. F. Yang, J. Ma, Synchronization and energy balance of star network composed of photosensitive neurons, *Eur. Phys. J. Spec. Top*., **231** (2022), 4025–4035. https://doi.org/10.1140/epjs/s11734-022-00698-0
12. G. Huang, S. Zhou, R. Zhu, Y. Wang, Y. Chai, Effect of internal and external chaotic stimuli on synchronization of piezoelectric auditory neurons in coupled time-delay systems, *Cogn. Neurodyn.*, **18** (2024), 2111–2126. https://doi.org/10.1007/s11571-023-10042-4
13. Y. Xu, J. Ma, Control of firing activities in thermosensitive neuron by activating excitatory autapse, *Chin. Phys. B*, **30** (2021), 100501. https://doi.org/10.1088/1674-1056/abeeef
14. G. Sun, Y. Xu, W. Jin, G. Ren, Energy balance regulates synchronization of photosensitive neural network, *Phys. A Stat. Mech. Appl*., **625** (2023), 129003. https://doi.org/10.1016/j.physa.2023.129003
15. L. Zhang, L. Xiong, X. An, Q. Shi, Hamilton energy balance and synchronization behaviors of two functional neurons, *Cogn. Neurodyn*., **17** (2023), 1683–1702. https://doi.org/10.1007/s11571-022-09908-w
16. Y. Xie, J. Ma, How to discern external acoustic waves in a piezoelectric neuron under noise? *J. Biol. Phys*., **48** (2022), 339–353. https://doi.org/10.1007/s10867-022-09611-1
17. Y. Guo, C. Wang, Z. Yao, Y. Xu, Desynchronization of thermosensitive neurons by using energy pumping, *Phys. A Stat. Mech. Appl*., **602** (2022), 127644. https://doi.org/10.1016/j.physa.2022.127644
18. Y. Xu, J. Ma, Pattern formation in a thermosensitive neural network, *Commun. Nonlinear Sci. Numer. Simul.*, **111** (2022), 106426. https://doi.org/10.1016/j.cnsns.2022.106426

19. Q. Shi, L. Zhang, X. An, L. Xiong, F. Yang, Dynamic exploration of a controllable thermosensitive neuron model and its applications, *Int. J. Bifurcation Chaos*, **32** (2022), 2250198. https://doi.org/10.1142/S021812742250198X
20. Q. Shi, S. Qu, X. An, X. Du, A novel coupled functional neuron model and its application in medical image encryption, *Nonlinear Dyn.*, **112** (2024), 11447–11470. https://doi.org/10.1007/s11071-024-09634-4
21. X. An, L. Jiang, L. Xiong, J. Zhang, X. Li, Synchronization behavior and energy evolution in physical neuron and network, *Nonlinear Dyn.*, **112** (2024), 16389–16407. https://doi.org/10.1007/s11071-024-09882-4
22. Y. Xie, P. Zhou, J. Ma, Energy balance and synchronization via inductive-coupling in functional neural circuits, *Appl. Math. Model.*, **113** (2023), 175–187. https://doi.org/10.1016/j.apm.2022.09.015
23. Y. Wang, F. Min, Y. Cheng, Y. Dou, Dynamical analysis in dual-memristor-based FitzHugh-Nagumo circuit and its coupling finite-time synchronization, *Eur. Phys. J. Spec. Top.*, **230** (2021), 1751–1762. https://doi.org/10.1140/epjs/s11734-021-00121-0
24. F. Yang, Z. Han, G. Ren, Q. Guo, J. Ma, Enhance controllability of a memristive neuron under magnetic field and circuit approach, *Eur. Phys. J. Plus*, **139** (2024), 534. https://doi.org/10.1140/epjp/s13360-024-05364-z
25. M. Ge, K. Jia, X. Wang, Y. Liu, Y. Jiang, Researches on dynamics and noise effects of FHN neuron based on memristor-memcapacitor coupling, *Nonlinear Dyn.*, **113** (2025), 26671–26693. https://doi.org/10.1007/s11071-025-11454-z
26. X. Zhou, K. Sun, H. Wang, Z. Yao, Coexisting hyperchaos and multistability in a discrete memristor-coupled bi-neuron model, *Nonlinear Dyn.*, **112** (2024), 9547–9561. https://doi.org/10.1007/s11071-024-09546-3
27. X. Li, W. Guo, Y. Du, Dynamical analysis and circuit implementation of HR-FHN neuron model coupled by locally active memristor, *Int. J. Bifurcation Chaos*, **34** (2024), 2430034. https://doi.org/10.1142/S0218127424300349
28. X. Zhang, J. Ma, Wave filtering and firing modes in a light-sensitive neural circuit, *J. Zhejiang Univ. Sci. A*, **22** (2021), 707–720. https://doi.org/10.1631/jzus.A2100323
29. P. Zhou, J. Ma, Y. Xu, Phase synchronization between neurons under nonlinear coupling via hybrid synapse, *Chaos Solitons Fractals*, **169** (2023), 113238. https://doi.org/10.1016/j.chaos.2023.113238
30. D. Yu, G. Wang, T. Li, Q. Ding, Y. Jia, Filtering properties of Hodgkin-Huxley neuron on different time-scale signals, *Commun. Nonlinear Sci. Numer. Simul.*, **117** (2023), 106894. https://doi.org/10.1016/j.cnsns.2022.106894
31. A. Brughera, J. A. Ballestero, D. McAlpine, Sensitivity to envelope interaural time differences: Modeling auditory modulation filtering, *J. Assoc. Res. Otolaryngol.*, **23** (2022), 35–57. https://doi.org/10.1007/s10162-021-00816-0
32. O. Abdalla, A. Y. Baran, N. Korkmaz, R. Kılıç, Investigation of synchronization control of the memristive/resistive-coupled neural network with noise effect, *Int. J. Bifurcation Chaos*, **34** (2024), 2450099. https://doi.org/10.1142/S0218127424500998
33. S. Hariharan, R. Suresh, V. K. Chandrasekar, Heterogeneous noise-induced extreme events and synchronization in a globally coupled network of FitzHugh-Nagumo oscillators, *Chaos Solitons Fractals*, **203** (2026), 117652. https://doi.org/10.1016/j.chaos.2025.117652

34. M. Akhmet, K. Başkan, C. Yeşil, Markovian noise-induced delta synchronization approach for Hindmarsh-Rose model, *Chaos Solitons Fractals*, **185** (2024), 115155. https://doi.org/10.1016/j.chaos.2024.115155
35. J. Huang, C. Li, T. Huang, Q. Han, Lag quasisynchronization of coupled delayed systems with parameter mismatch by periodically intermittent control, *Nonlinear Dyn.*, **71** (2013), 469–478. https://doi.org/10.1007/s11071-012-0673-y

AIMS Press